

## Evaluation of Surface Temperature and Emissivity Derived from ASTER Data: A Case Study Using Ground-Based Measurements at a Volcanic Site

ÁFRICA BARRETO, MANUEL ARBELO, PEDRO A. HERNÁNDEZ-LEAL, AND LAIA NÚÑEZ-CASILLAS

*Grupo de Observación de la Tierra y la Atmósfera (GOTA), Departamento de Física FEES, Universidad de La Laguna, La Laguna, Tenerife, Spain*

MARÍA MIRA AND CÉSAR COLL

*Department of Earth Physics and Thermodynamics, University of Valencia, Valencia, Spain*

(Manuscript received 21 January 2010, in final form 13 May 2010)

### ABSTRACT

The land surface temperature (LST) and emissivity (LSE) derived from Advanced Spaceborne Thermal Emission and Reflection Radiometer (ASTER) data were evaluated in a low spectral contrast volcanic site at an altitude of 2000 m on the island of Tenerife, Spain. The test site is almost flat, thermally homogeneous, and without vegetation cover or variation in its surface composition. ASTER data correspond to six scenes, under both day- and nighttime conditions during 2008. This case study analyzes the impacts of the sources of inaccuracies using the temperature–emissivity separation (TES) algorithm. Uncertainties associated with inaccurate atmospheric correction were minimized by means of local soundings and the climate advantages of the area.

Concurrent ground-based radiometric measurements were performed for LST, and laboratory and field measurements for LSE, to obtain reference values. The TES evaluation showed a good level of agreement in the emissivity derived for ASTER bands 13 and 14 [root-mean-square difference (RMSD) lower than 0.002] and discrepancies in ASTER bands 10 and 11 that were within the expected performance of the algorithm ( $\pm 0.015$ ). However, out-of-threshold errors were retrieved in band 12, producing an artificial increase in spectral contrast. The underestimated TES LSE spectra point to the presence of a roughness effect at measurement scales that may increase the laboratory band emissivity values. TES LST comparison with ground data showed an RMSD value of 0.5 K. ASTER standard products AST08 (LST) and AST05 (LSE) atmospherically corrected by means of Naval Research Laboratory (NRL) data were also tested, showing a similar level of performance for the TES implemented with local soundings, but failed in high-humidity atmospheric conditions.

### 1. Introduction

Land surface temperature (LST) is a key variable for global climate and environmental change studies because it controls the fluxes of energy and water between the atmosphere and the land surface.

High-resolution thermal infrared (TIR) remote data provide a unique opportunity to derive thermally emitted radiance information from the land surface and, therefore, to extract global and continuous LST information. The Advanced Spaceborne Thermal Emission and Reflection Radiometer (ASTER), on board the

*Terra* satellite, has been an important contribution to TIR remote sensing. ASTER contains five channels in the thermal infrared range with a spatial resolution of 90 m and a radiometric resolution ( $NE\Delta T$ ) of less than 0.3 K at 300 K.

The use of infrared radiometry to estimate LST has uncertainties due to two main factors: 1) the atmospheric effects on the radiance measured by the sensor (mainly by water vapor absorption and reemission processes) and 2) the uncertainty in land surface emissivity (LSE). A number of approaches focused on determining LST and LSE accurately from satellite data have been developed to overcome these effects.

The temperature and emissivity separation (TES) algorithm (Gillespie et al. 1998) is usually used to extract surface temperature and emissivity from ASTER data.

---

*Corresponding author address:* África Barreto, Dept. de Física FEES, Universidad de La Laguna, 38206 La Laguna, Spain.  
E-mail: afriba@ull.es

It uses an empirical relationship to predict minimum emissivity  $\epsilon_{\min}$  from the surface spectral contrast, defined as the difference between maximum and minimum emissivities (MMD). It was determined by Gillespie et al. (1998) from laboratory measurements using a large number of natural samples. As Coll et al. (2007) suggest, it has been proven to underestimate emissivity in the case of low spectral contrast surfaces, being a source of inaccuracies in itself. As shown in Coll et al. (2007) and Gustafson et al. (2006), TES tends to amplify any external error, such as those introduced by an inaccurate sensor calibration, atmospheric correction, measurement errors, or problems in the algorithm itself, mainly in  $\epsilon_{\min}$  versus MMD regression. Coll et al. (2007) also include the surface heterogeneities viewed at ASTER scales as other possible sources of error. This occasional failure is expected to occur at high atmospheric temperatures, low-elevation sites, and under conditions of atmospheric water vapor content greater than  $1.7 \text{ g cm}^{-2}$  (Jimenez-Muñoz et al. 2006). Due to the difficulty in finding a land site suitable for validation experiments located at high altitude and minimally affected by atmospheric absorption/emission processes, the greater part of the validation studies in the literature are referred to low-elevation sites, and, thus, more susceptible to errors in atmospheric characterization.

The main goal of this case study is to evaluate the accuracy of LST and LSE derived from ASTER-TIR data acquired over a high-elevation volcanic site with low spectral contrast, located in Tenerife, Canary Islands, Spain. Since a large number of validation protocols have been developed to account for ASTER LST and/or LSE accuracy (e.g., Coll et al. 2007; Jimenez-Muñoz et al. 2006; Sabol et al. 2009), this particular validation exercise attempts to reduce the impacts of the external sources of error on the surface parameters. This objective will be achieved by 1) ensuring the minimum effects of ASTER calibration inaccuracies, 2) improving atmospheric correction through the use of local atmospheric profiles and the selection of a validation site at an altitude minimally affected by atmospheric water vapor, and 3) ensuring the spatial and temporal homogeneity of the test site at the ASTER scales.

To this end, ASTER scenes for 4 days and 2 nights were acquired, coincident with radiometric ground measurements collected as a part of a field campaign performed during the spring and summer of 2008. We used the level 1B (L1B) products and applied an atmospheric correction using a radiative transfer code with local sounding data to retrieve surface parameters by means of the TES algorithm. We then intercompared these results with the ASTER standard products obtained from the Earth Remote Sensing Data Analysis Center (ERSDAC).

This paper follows with the physical basis of the temperature and emissivity determination. The main characteristics of the validation area selected (i.e., spatial location, atmospheric features, composition, and thermal homogeneity) are shown in section 3. In section 4 ASTER data, the TES algorithm, and ground measurements involved in the field campaign are presented. The methodology involved in the emissivity determination and instrumentation is also described. Finally, the main results of the comparison between ground, ASTER TES, and standard products are given, as well as the general conclusions of the study.

## 2. Physical framework for LST and LSE determination

The TES algorithm is based on the radiative transfer equation. In the TIR region, where the reflected solar radiation is much smaller than the earth emission, the approximation of the Lambertian surface can be assumed. Hence, the radiative transfer equation can be written as (Hook et al. 2007)

$$L_{\text{sensor},j} = [\epsilon_j B_j(T_{\text{surf}}) + (1 - \epsilon_j) L_j^{\downarrow}] \tau_j + L_j^{\uparrow}, \quad (1)$$

where  $L_{\text{sensor},j}$  represents the at-sensor radiance measured by ASTER in channel  $j$ . This magnitude depends directly on atmospheric parameters  $\tau_j$ ,  $L_j^{\downarrow}$ , and  $L_j^{\uparrow}$ , where  $\tau_j$  represents the spectral atmospheric transmittance,  $L_j^{\downarrow}$  is the spectral upwelling radiance (path radiance), and  $L_j^{\uparrow}$  is the spectral atmospheric downwelling radiance. In addition,  $B_j$  is the blackbody radiance of a surface at temperature  $T_{\text{surf}}$  and  $\epsilon_j$  is the spectral surface emissivity.

From Eq. (1) the radiance at ground level ( $L_{\text{ground},j}$ ) is given by

$$L_{\text{surf},j} = \epsilon_j B_j(T_{\text{surf}}) + (1 - \epsilon_j) L_j^{\downarrow}, \quad (2)$$

where the surface radiance is the term  $\epsilon_j B_j(T_{\text{surf}})$ .

Even when  $L_{\text{ground},j}$  is known,  $\epsilon_j$  and  $T_{\text{surf}}$  cannot be derived due to the temperature and emissivity coupling. Thus, any methodology that attempts to decouple the surface temperature and emissivity from Eq. (2) needs additional information, which may be a source of uncertainties in itself. Its success depends on the ability of the new equation to reliably reproduce the physics of the temperature and emissivity relation for the surface under study.

The accurate estimation of the atmospheric contribution from input variables such as temperature, water vapor, or ozone content is also required. Since these variables are prone to introducing important discrepancies due to their high spatial and temporal variations, the use

of local vertical profiles and highly elevated sites is considered the ideal method of better characterizing the atmosphere at the time of measurement. Unfortunately, many problems arise when selecting an elevated land site suitable for use as a validation area, and numerous validation studies in the literature are referred to low-altitude sites (e.g., Coll et al. 2005, 2007; Jimenez-Muñoz et al. 2006).

Other important errors related to sensor calibration or the test area also can affect the LST and LSE accuracy. The first-mentioned errors will be discussed in section 4. The next type of difficulty is basically encountered due to the presence of heterogeneities in the surface composition or irregularities of the area. The most common problems are related to surface roughness, the impacts of which can be observed at a variety of scales (Kirkland et al. 2002), from small scales, where a cavity effect may be introduced, and thus a lower emissivity spectral contrast, to large scales, through surface macroroughness or nonflat areas, which often cause shadowing problems (lower pixel-averaged temperature) and a cavity effect also. These problems may produce temperature and emissivity variations within a pixel, an artificial flat emissivity spectrum, and, therefore, discrepancies between the different batches of spatial resolution information.

All these effects imply an especially challenging task when retrieving and validating LST and LSE from remotely sensed data, and force us to select study sites where they are minimized.

### 3. Study area

The selected area is a spatial and thermally homogeneous site where uncertainties associated with inaccurate atmospheric correction will be minimized by using local atmospheric profiles and the climatic advantages of a high altitude site.

#### *a. Test site location: Composition, temporal, and spatial homogeneity*

Tenerife is the largest of the seven Canary Islands, a volcanic archipelago located about 115 km west of the African coast in the North Atlantic Ocean. The Tenerife test site is a volcanic area of 4.9 km<sup>2</sup> situated inside the Las Cañadas complex at an altitude of 2000 m, in the so-called Mount Chahorra coulee (see Fig. 1). It presents several advantages that make it suitable for serving as a validation test area, being composed of tephriphonolite lava, homogeneous, and almost flat. A whole rock geochemical analysis developed by Ablay et al. (1998) shows this lava has a silicon dioxide (SiO<sub>2</sub>) content of 49.53%



FIG. 1. Photograph of the Mount Chahorra site (Tenerife Island) with the 1798 lava flow from the western flank of Pico Viejo covering a homogeneous and nearly flat area inside Las Cañadas del Teide National Park.

in weight. It does not present vegetation cover or variation in its surface composition, ensuring the temporal and spatial homogeneity of the site. Moreover, the site is large enough to validate remote information, with a spatial resolution from meters to some kilometers.

Figure 2a shows the site location within Tenerife Island, which coincides with the 11 × 11 ASTER pixels characterized in the zoom image of Fig. 2b with a yellow box. Ground measurements were performed in an area of about 1 km<sup>2</sup>, as indicated with a star, centered at 28°13'51"N, 16°41'26"W.

#### *b. Atmospheric features*

The Canary Islands are influenced by trade winds, which imply a typical atmospheric vertical structure that maintains the greater part of the atmospheric water vapor concentrated under a mean altitude of 1500 m (from 1730 m in wintertime to 1270 m in summertime). As a result, areas of Tenerife at high elevation have a generally low total column water vapor due to being above the moisture-laden stratum. In particular, the test site, at the Las Cañadas del Teide National Park, located in the central part of the island at a mean altitude of 2000 m above mean sea level (MSL) and dominated by the Pico Teide (3718 m), is a good location for minimizing the atmospheric influence on remote sensing data.

A thorough atmospheric characterization of the test site was developed to account for the impacts of the atmospheric correction on the remote data. A total of 317 cloud-free local atmospheric profiles obtained from January 2006 to April 2008 show a mean value of 0.44 g cm<sup>-2</sup> for the total column water vapor in the test site. They were introduced in the Moderate Resolution

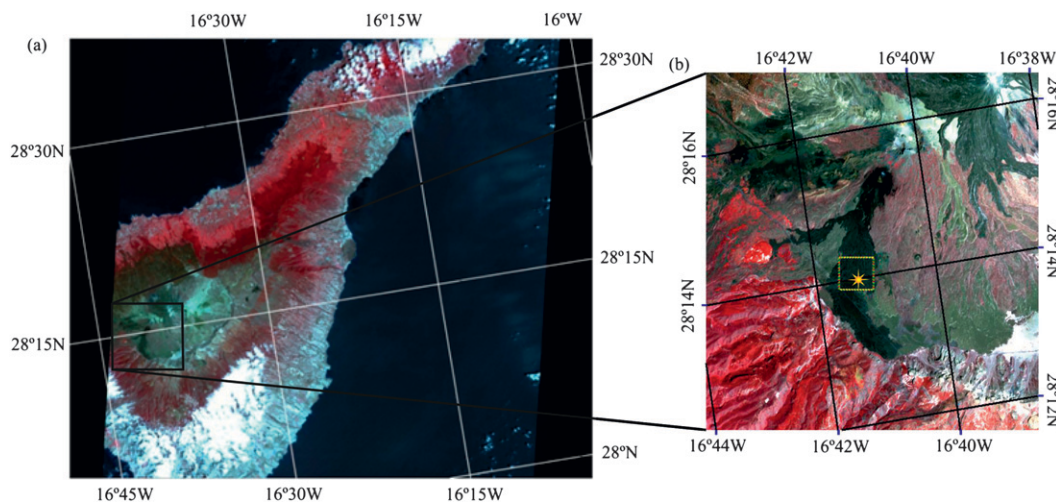


FIG. 2. (a) ASTER color composite for 16 Apr 2008. RGB components are band 3 ( $0.81 \mu\text{m}$ ), 2 ( $0.66 \mu\text{m}$ ), and 1 ( $0.56 \mu\text{m}$ ), respectively. (b) Zoom image centered on the  $11 \times 11$  pixel validation site (yellow box). A  $1\text{-km}^2$  ground measurements area within validation area is marked with a star.

Atmospheric Transmission (MODTRAN) radiative code (Berk et al. 1999) to retrieve the representative values of  $\tau_j$ ,  $L_j^\uparrow$ ,  $L_j^\downarrow$ , and at-sensor radiances ( $L_{\text{sensor}}$ ) corresponding to a layer at an altitude of 2000 m. The main results are shown in Table 1. For  $\tau_j$ , we found a mean increase in our test site relative to the value at the surface level, ranging from 37.1% in band 10 to 16.5% in band 12. Regarding  $L_j^\uparrow$  and  $L_j^\downarrow$ , the most notable reduction was retrieved in bands in the lower-wavelength region (bands 10–12), precisely the ones more affected by water vapor absorption. In the higher-wavelength region (bands 13 and 14), we obtained a decrease in these parameters lower than 16.1%.

Despite the expected reduction in the atmospheric effects due to the greater altitudes, two relevant issues are seen in these results. The first one is the notable increase in atmospheric transmission for the bands that are more affected by the water vapor absorption effect (bands 10 and 11), while band 12 presents the lowest rise. The second issue is related to the decrease in the atmospheric downward radiation effect ( $L_j^\downarrow$ ) on remote data. This is a relevant term in the radiative transfer equation because the radiation measured by the sensor contains not only the radiation emitted by the surface but that reflected by the surface [Eq. (2)]. Since it acts by reducing the spectral contrast (Hook et al. 2007), an inaccurate estimation of this term may yield an incorrect LSE and, therefore, an erroneous LST estimation.

### c. Thermal homogeneity

ASTER brightness temperatures were used to check the thermal homogeneity of the test site. Data from six images acquired on 2 February 2003, 15 September

2005, 26 March 2006, 1 June 2006, 31 March 2008, and 16 April 2008 were analyzed. Band 10 ( $8.125\text{--}8.475 \mu\text{m}$ ) was selected according to the lowest thermal variability found in this spectral range for the volcanic area. Table 2 shows temperature statistics for the days involved in the study. Considering the  $11 \times 11$  pixel area, a mean standard deviation ( $\bar{\sigma}$ ) for the whole period smaller than 0.5 K was found (Table 2). This value ensures thermal homogeneity at ASTER scales ( $90 \text{ m} \times 90 \text{ m}$ ) and discards the effects of shadowing or thermal inertia on the nearby pixels at this spatial resolution.

## 4. Data and methodology

### a. ASTER data and TES algorithm

The ASTER sensor, on board National Aeronautics and Space Administration's (NASA) *Terra* satellite, provides 90-m resolution in its five thermal infrared bands (10–14), between 8 and  $12 \mu\text{m}$ . Digital numbers (DNs) were obtained from Level 1B information for six scenes, four daytime (16 April, 2 May, 19 June, and 5 July 2008) and two nighttime (9 and 18 August 2008), centered on

TABLE 1. Reduction of atmospheric parameters (expressed in %) at a site located at 2000 m MSL relative to a sea level site for the five ASTER TIR bands, including the effective wavelength.

ASTER band	$\tau_j$	$L_j^\uparrow$	$L_j^\downarrow$
Band 10 ( $8.291 \mu\text{m}$ )	37.1	29.4	31.0
Band 11 ( $8.634 \mu\text{m}$ )	22.9	27.5	28.7
Band 12 ( $9.075 \mu\text{m}$ )	16.5	22.6	23.4
Band 13 ( $10.657 \mu\text{m}$ )	20.1	15.3	16.1
Band 14 ( $11.318 \mu\text{m}$ )	24.6	13.3	13.9

TABLE 2. Band 10 brightness temperatures statistics for  $11 \times 11$  pixels over the validation site for each day: minimum ( $T_{\min}$ ), maximum ( $T_{\max}$ ), average ( $T_{\text{avg}}$ ), and standard deviation ( $\sigma$ ).

Day	$T_{\min}$ (K)	$T_{\max}$ (K)	$T_{\text{avg}}$ (K)	$\sigma$ (K)
2 Mar 2003	296.89	299.56	298.13	0.57
15 Sep 2005	303.36	307.02	304.57	0.51
26 Mar 2006	301.87	305.31	303.08	0.55
1 Jun 2007	308.52	310.83	309.48	0.41
31 Mar 2008	299.81	301.94	300.58	0.39
16 Apr 2008	303.15	305.63	304.30	0.37
Average	—	—	—	0.46

Tenerife Island. These data can be converted to radiances using the unit conversion coefficients (UCCs) and the radiometric calibration coefficients (RCCs). These values are based on prelaunch integrating sphere observations (Arai 2005), but it has been demonstrated that the periodical updating does not follow the sensor degradation rate (Tonooka et al. 2004). Indeed, Tonooka et al. (2004) found a major reduction in the sensor response of band 12, up to 80% since the launch, while in band 10 the degradation is the slowest. These authors therefore introduced a user-based recalibration method for level-1 products that updates the RCCs in the case of calibration errors exceeding the thresholds of 0.5 K at 300–320 K or 1 K at 340 K (Tonooka et al. 2005). This method managed to reduce calibration inaccuracies for RCC version 2.09 or later, but was unable to reduce them in some versions, particularly in version 2.05 and 2.06 products. Recent products calibrated by RCC versions 3.00 or later are able to maintain the error within the threshold of the ASTER–TIR radiometric noise by means of a day-by-day regressive method developed by Sakuma et al. (2005). Since the scenes we used were calibrated by recent RCC versions (3.07 for the first 3 days, and 3.08 for the last 3 days), they are considered to be sufficiently accurate and their errors within the threshold of NE $\Delta$ T.

Atmospheric parameters were estimated by means of near-concurrent atmospheric profiles measured at a sounding station of the Spanish Meteorology Agency located about 10 km from the test site, launched at 1200 and 0000 UTC (ASTER overpass times of 1153 and 2353 UTC), and extracted from the Department of Atmospheric Science of the University of Wyoming Web site (<http://weather.uwyo.edu/upperair/sounding.html>). They were used as input to the MODTRAN 3.5 radiative code. The output of this code must be integrated over the response function of each ASTER band in order to obtain the spectral parameters ( $\tau_j$ ,  $L_j^\uparrow$ ,  $L_j^\downarrow$ ). The use of local atmospheric profiles (pressure, temperature, and humidity) ensures a suitable characterization of atmospheric conditions at the times of satellite measurement.

We have extracted from them a water vapor column (from an altitude of 2000 m MSL) of 0.32, 0.48, 0.32, 0.42, 1.33, and 0.65 g cm $^{-2}$ , respectively, for the 6 days.

LST and LSE are determined through our implementation of the TES algorithm from the ASTER at-sensor radiances [Eq. (1)]. The TES algorithm solves the temperature and emissivity coupling from Eq. (2) by using a sequence of three modules: NEM (normalized emissivity method), RATIO, and MMD. First, the NEM module is used to estimate the surface temperature from atmospherically corrected radiances. It assumes a constant emissivity,  $\varepsilon_{\text{NEM}}$ , in all  $j$  channels for a given pixel, retrieving  $j$  brightness temperatures ( $T_j$ ). The highest of these temperatures is used as the surface temperature,

$$T_{\text{surf}} = \max(T_j), \quad (3)$$

and band emissivities  $\varepsilon_j$  are then computed:

$$\varepsilon_j(T_{\text{surf}}) = \frac{L_{\text{surf},j} - L_j^\downarrow}{B_j(T_{\text{surf}}) - L_j^\downarrow}, \quad (4)$$

which yields surface emissivity spectra ( $\varepsilon_j$ ). In the RATIO module, we used these estimations to generate a ratio emissivity spectrum ( $\beta_j$ ), which preserves the shape but not the amplitude, by means of the following expression:

$$\beta_j = \frac{\varepsilon_j B_j \overline{B_j(T)}}{B_j(T) \overline{\varepsilon_j B_j}}. \quad (5)$$

The MMD module is used to recover its amplitude, and the final emissivity spectrum is obtained by using the following empirical relation extracted from laboratory measurements:

$$\varepsilon_{\min} = (0.994 - 0.687)\text{MMD}^{0.737}, \quad (6)$$

from (6), we thus obtain the surface temperature.

We did not consider the iterative process proposed by Gillespie et al. (1998) in the NEM module for removing the reflected sky irradiance since it has been recently considered unsatisfactory by Gustafson et al. (2006). They found that the iteration in the TES algorithm can lead to erroneously low final emissivity estimates due to the nonconvergence of the procedure.

#### b. Ground measurements

In situ surface temperature measurements were carried out within the test site as a part of a field campaign developed by the research groups of La Laguna and Valencia Universities. Ground measurements were concurrent with the ASTER overpasses to compare in

situ and satellite-derived data under similar atmospheric conditions.

We used four infrared radiometers: two CIMEL 312 models, with four (8–13, 11.5–12.5, 10.3–11.3, and 8.2–9.2  $\mu\text{m}$ ) and six (8–14, 11–11.7, 10.3–11, 8.9–9.3, 8.5–8.9, and 8.1–8.5  $\mu\text{m}$ ) spectral bands, hereafter CE1 and CE2, and two AGEMA Thermopoint Model 80s, with one single broad band (8–14  $\mu\text{m}$ ), denoted as AGA1 and AGA2. Both CE1 and CE2 are radiance-based thermal infrared radiometers. They have a field of view (FOV) of  $10^\circ$  and a response time of 1 s. The AGA thermometers each have a FOV of  $2^\circ$ .

Surface temperature was extracted using band 1 of both CE1 and CE2 exclusively, with a spectral range similar to that of the two AGAs, to ensure the comparability between IR radiometers. Meanwhile, for emissivity measurements, the six bands of CE2 were used in order to retrieve the spectral variation of the surface emissivity. Since this instrument has five spectral bands approximately coincident with the ASTER TIR bands (bands 2–6 of CE 312–2), measurements can be used for validating the ASTER TES surface emissivity.

Instruments were previously calibrated and intercalibrated using a traceable primary calibration blackbody in order to check the comparability between instruments and correct for any possible bias in their readings that could introduce inaccuracies in the measured LST. Moreover, the accuracy of each instrument was regularly checked during the field campaign. We obtained absolute accuracies of 0.1 and 0.2 K, respectively, for the CE1 and CE2 broad bands. These results show the good performance of CIMEL IR radiometers, verifying accuracies specified by previous authors (Legrand et al. 2000). However, lower accuracies were retrieved for AGA1 ( $\pm 0.4$  K) and AGA2 ( $\pm 0.5$  K).

Temperature measurements were performed at regular steps through four transects over well-defined areas (one per instrument) within the validation site to span a large part of this area, sampling LSTs 30 min before and after satellite overpass. Although only temperature data in a range of  $\pm 5$  min around the satellite overpass were considered when calculating the ground LST, this time interval allows us to account for the spatial and temporal variabilities of the surface temperature ( $\sigma_{\text{VAR}}$ ), as will be shown in section 5. These  $\sigma_{\text{VAR}}$  values may oscillate greatly due to wind conditions. We therefore conducted in situ wind measurements using a cup anemometer during surface measurements, observing a daily average wind speed that did not exceed  $2.9 \text{ m s}^{-1}$  (3.0, 3.2, 2.4, 3.1, 0.6, and  $5.1 \text{ m s}^{-1}$ , respectively, for the 6 days). No significant wind gusts were observed during the field campaign.

In situ radiometric measurements were performed by the four instruments placed at a height of 150 cm above

the ground in a close-to-nadir view. Sky emission was also measured at least 3 times during the temperature transect (at the start, middle, and end) to account for the downwelling sky irradiance terms in Eqs. (1) and (2).

### c. Determination of surface emissivity

Laboratory and in situ measurements were performed to estimate the land surface emissivity with CE2. This a priori information provides an emissivity reference to be used as TES algorithm input, and for comparison with ASTER TES LSE and emissivity from ASTER standard product AST05. To this end, we used the two-lid version of the box method. A thorough description of this procedure is given by Rubio et al. (2003). It is a controlled experiment that isolates the sample from its surroundings. Without external contributions, we can determine the radiation coming up to the radiometer from the bottom of the box and therefore estimate the directional emissivity of elemental surfaces. The experimental device consists of a rectangular bottomless box with polished aluminum inner sides (reflectivity close to unity), which ensures no contribution from the walls to the signal reaching the sensor from the sample. The device was covered with a thermal insulator to ensure thermal stability inside the box during the measurements. Two lids are also required: one cold lid made of polished aluminum and one hot lid painted in black coating (Nextel velvet black coating 811–21), which is often used for calibration sources (emissivity close to unity). A resistive circuit allows us to reach high temperatures in the hot lid, controlled by a thermostat. Sample temperature should remain constant and at least  $30^\circ\text{C}$  below the hot lid temperature. It is also required that measurements be made sufficiently quickly to avoid causing temperature differences inside the box and, thus, their being affected by adverse environmental conditions (strong insolation, wind conditions, etc.) in the case of field measurements.

This method accomplishes a series of four radiometric measurements per channel and sample. All of them involve exchanging the two lids at the top of the box, placing the sample or a cold lid at the bottom. At this point, it is important to mention that 20 emissivity estimations were conducted per channel and sample, considering the average value to be the surface emissivity. Thus, a total of 120 groups of four radiometric measurements were carried out per sample.

We retrieved seven emissivity spectra of the volcanic rock: three of them obtained from in situ measurements in different areas of the volcanic site and four more in the laboratory by means of four representative samples extracted from this area. This helped us to detect discrepancies due to environmental conditions or the lack

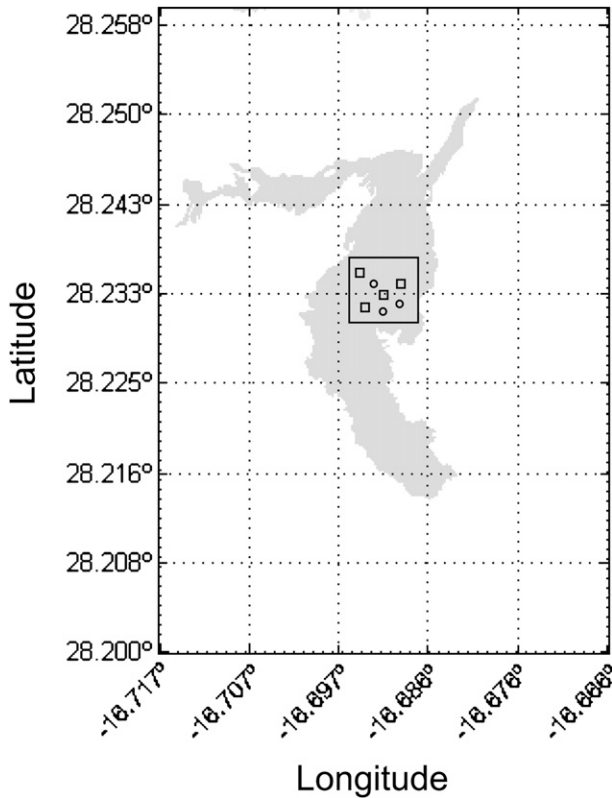


FIG. 3. Circles indicate the locations in the Mount Chahorra area of in situ emissivity measurements, and squares show the places where emissivity samples were extracted for laboratory measurements.

of representativeness of the laboratory sample, ensuring the spatial stability and representativeness of the emissivity spectrum obtained. Figure 3 shows the locations (circles) of the three different areas where emissivity measurements were performed within the  $11 \times 11$  ASTER pixel validation area and also the places where representative samples were extracted to be measured at the laboratory (squares). Temporal variations of surface emissivity are minimized since the composition of the site remains unaltered, it has no vegetation cover that could alter the surface properties, and the environmental conditions did not change appreciably during the field measurements.

## 5. Results and discussion

### a. Surface emissivity

From laboratory and field measurements described in the previous section, an average spectral emissivity for tephriphonolite lava of  $0.973 \pm 0.002$  (8–14  $\mu\text{m}$ ),  $0.970 \pm 0.006$  (11.0–11.7  $\mu\text{m}$ ),  $0.969 \pm 0.007$  (10.3–11.0  $\mu\text{m}$ ),  $0.966 \pm 0.005$  (8.9–9.3  $\mu\text{m}$ ),  $0.969 \pm 0.006$  (8.5–8.9  $\mu\text{m}$ ),

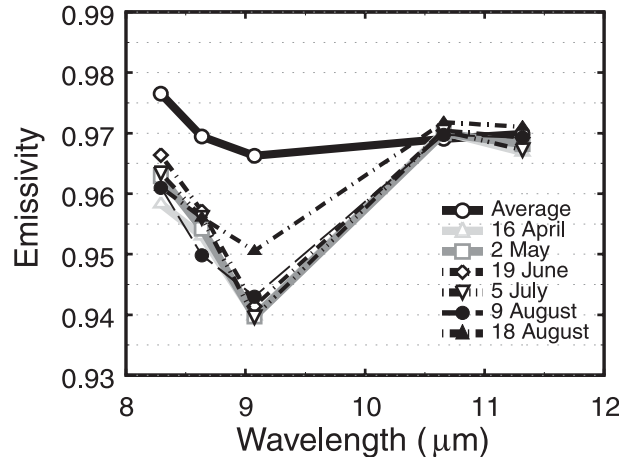


FIG. 4. Test site spectral emissivity obtained by means of the TES algorithm for each day and the average spectrum obtained from laboratory and field measurements.

and  $0.976 \pm 0.005$  (8.1–8.5  $\mu\text{m}$ ) for CE2 bands 1–6, respectively, was retrieved. The band uncertainty is determined as the maximum error associated with the propagation of uncertainties in each measurement and experiment. It should be noted that there are no significant discrepancies between the spectra obtained, showing a standard deviation ranging from 0.003 (band 3) to 0.001 (band 6). From these results, we can assume that the average spectrum is representative of the test site, discarding important experimental or representative errors. Therefore, the tephriphonolite lava used in this study presents a high-emissivity spectrum characterized by low spectral variation, with an amplitude lower than 0.01, on the order of the uncertainties involved in the method of measurement.

This average surface emissivity was compared to those retrieved by means of the ASTER TES algorithm, applied to ASTER data for 6 days assuming an NEM emissivity of 0.97, which is close to the measured emissivity spectra.

Figure 4 shows an emissivity spectral contrast that is higher than expected for all days (about 0.03 for the daytime data and 0.027 and 0.021 for the two night scenes). These differences, as well as the RMSDs of the emissivity differences, are shown for each ASTER band in Table 3. The TES method provides a good level of agreement for the emissivity derived for ASTER band 13 (0.001) and band 14 (0.002). For the remaining bands, which are more affected by water vapor absorption processes, we found fluctuations of 0.014 for band 10 and 0.015 for band 11, which are within the  $\pm 0.015$  value of the standard performance of the ASTER TES and the accuracy expected for the laboratory-extracted emissivity spectra (section 4c). However, an important difference

TABLE 3. Differences between surface emissivities measured with CE2 and the box method and those obtained for each ASTER band from the TES algorithm for the 6 days.

Day	Band 10	Band 11	Band 12	Band 13	Band 14
16 Apr	0.018	0.016	0.026	-0.001	0.003
2 May	0.014	0.015	0.027	-0.001	0.002
19 Jun	0.010	0.012	0.025	-0.001	0.000
5 Jul	0.013	0.013	0.027	-0.001	0.003
9 Aug	0.015	0.020	0.023	-0.001	0.001
18 Aug	0.015	0.013	0.016	-0.003	-0.001
RMSD	0.014	0.015	0.024	0.001	0.002

was found for band 12 (from 0.016 to 0.027), which was found to be always larger than this uncertainty threshold. As described in section 3b, band 12 is precisely the less favored by the altitude of the site. This would imply a higher impact of atmospheric inaccuracies on band 12. In addition to the ASTER TIR calibration problem, the rapid reduction in band 12's response, discussed in section 4a, can certainly affect the emissivity retrieved, even when the scenes were calibrated by means of Sakuma's method (Sakuma et al. 2005). Thus, in agreement with Sabol et al. (2009), this unexpected performance can be attributed to an inaccurate atmospheric correction or calibration errors, being responsible for the wavelength dependence of these differences. These uncertainties imply the propagation of radiometric noise inside the algorithm, having a profound impact on surfaces characterized by low spectral contrast. Since the uncertainties may be larger than the contrast itself, they produce larger MMD values in the TES-MMD module.

The fact that the ASTER TES LSE values in all bands are lower than the laboratory spectra (see Fig. 4) points to the presence of a roughness effect at the scales of the size of the rocks ( $\sim$ cm) and at the scales of roughs visible to naked eye ( $\sim$ mm to cm) (Kirkland et al. 2002), with more significant effects at the field and laboratory measurement scales than at ASTER ones. Its net effect is the

increase in the field and laboratory band emissivities. The effects of large-scale roughness (topography), which cannot be measured at laboratory scales, are discarded due to the fact that the site is characterized by nearly flat topography, the time of satellite measurements (taken at midday, when shadowing effects are minimum), as well as the fact that the site has been proven to be homogeneous at this scale (section 3c).

### b. Surface temperature

Values of 311.0, 312.4, 318.2, 317.0, 291.3, and 293.4 K were obtained for ASTER TES LST on 16 April, 2 May, 19 June, 5 July, and 9 and 18 August 2008, respectively. Field LSTs measured from each individual radiometer, as well as the weighted average temperature as a function of their accuracy ( $LST_{\text{ground}}$ ), are shown in Table 4.

The total uncertainty  $\sigma(T)$  over the ground temperature was obtained according to Coll et al. (2005):

$$\sigma(T) = [\sigma(\text{cal})^2 + \sigma(\varepsilon)^2 + \sigma(\text{VAR})^2]^{1/2}. \quad (7)$$

A combination of uncertainties can be associated with the three possible error sources involved in ground LST determination: calibration ( $\sigma_{\text{cal}}$ ), emissivity correction ( $\sigma_{\varepsilon}$ ), and spatial and temporal thermal variability ( $\sigma_{\text{VAR}}$ ) in validation measurements, which include information garnered within 5 min before and after satellite overpass. These values led to large uncertainties affecting  $LST_{\text{ground}}$  (Table 4). The major source of uncertainty in this term is introduced by spatial variations of the surface temperature ( $\sigma_{\text{VAR}}$ ) between 0.5 and 1.2 K for CE1 and CE2, and between 0.7 and 2.8 K for AGA1 and AGA2. The reason why large variations were observed in the experimental data may be attributed to the characteristics of the surface itself, which is bare and rugged, with cavities between individual rocks, and with regard to the time of measurements, taken at midday, when turbulence effects may be greater. Thus, despite being thermally homogeneous at ASTER scales (section 3c),

TABLE 4. Ground-measured ( $LST_{\text{ground}}$ ), ASTER/TES (LST), and ASTER/TES product AST08 ( $LST_{\text{SP}}$ ) temperatures for the validation site, including uncertainties in the measurements ( $\sigma$ ). Here,  $LST_{\text{ground}}$  is obtained through a weighted average of the broadband IR radiometers, according to its accuracy. The difference between the ground and ASTER/TES temperatures ( $\Delta LST$ ) is shown, as is that between the ground and ASTER/TES product temperatures ( $\Delta LST^*$ ).

Day	CE 1 (K)	CE 2 (K)	AGA 1 (K)	AGA 2 (K)	$LST_{\text{ground}}$ (K)	LST (K)	$\Delta LST$ (K)	$LST_{\text{SP}}$ (K)	$\Delta LST^*$
16 Apr	311.8 $\pm$ 1.2	311.1 $\pm$ 0.6	312.6 $\pm$ 1.6		311.4 $\pm$ 1.6	311.0	0.4	311.6	-0.2
2 May	313.9 $\pm$ 0.9	312.5 $\pm$ 0.8	312.3 $\pm$ 0.7	312.5 $\pm$ 2.2	313.5 $\pm$ 2.2	312.4	1.1	312.5	1.0
19 Jun		318.1 $\pm$ 0.5		318.4 $\pm$ 1.6	318.2 $\pm$ 1.5	317.9	0.3	319.0	-0.8
5 July		317.1 $\pm$ 0.7		316.9 $\pm$ 2.9	317.0 $\pm$ 2.9	317.1	-0.1	317.3	-0.3
9 Aug		292.4 $\pm$ 0.8		289.5 $\pm$ 1.0	291.3 $\pm$ 1.0	292.1	-0.8	292.6	-1.3
18 Aug		293.4 $\pm$ 0.7			293.4 $\pm$ 0.7	294.0	-0.5	292.6	0.8
RMSD							<b>0.5</b>		<b>0.8</b>

fluctuations are introduced at ground measurements scales.

According to Table 4, we obtained satellite-retrieved LST values that were very close to the ground measurements, in spite of the fact that the accuracy of the TES method is expected to decrease for a surface characterized by low MMD values (Jimenez-Muñoz et al. 2006). Differences in  $\Delta$ LST (ground minus TES) lower than 1.1 K (0.4, 1.1, 0.3,  $-0.1$ ,  $-0.8$ , and  $-0.5$  K) were retrieved for the 6 days, all of which were within the uncertainty window of  $\pm 1.5$  K established by Gillespie et al. (1998) and the equivalent noise temperature difference for the ASTER TIR bands. The RMSD of  $\Delta$ LST for the six ASTER scenes analyzed was approximately 0.5 K. In addition, these differences were at the same level of accuracy as the ASTER instrument and the thermal differences of the site found in section 3c at ASTER scales. The results were similar to those obtained by Coll et al. (2007) through a local adjustment of ASTER data. In addition, the reduced daily differences found are consistent with the low atmospheric humidity typical of the site due to its high elevation (as total column water vapor is always lower than  $1.3 \text{ g cm}^{-2}$ ) and are favored by the agreement found in satellite-retrieved emissivity for bands 13 and 14 centered at 10.65 and 11.31  $\mu\text{m}$ . These bands are located within the spectral range where the maximum emissivity of most natural surfaces occurs and the emissivity variability is the lowest. So, TES LST (defined as the maximum temperature of the five ASTER bands) will likely be retrieved in these bands, as is the case in this study, being affected by inaccuracies in LSE to a lesser extent.

### c. Comparison of ground and ASTER TES LST and LSE with ASTER standard products

We intercompared the ASTER TES LST, LSE, and ground measurements ( $LST_{\text{ground}}$  and laboratory spectrum) obtained in previous sections with ASTER standard products AST08 (earth surface temperature, i.e.,  $LST_{\text{SP}}$ ) and AST05 (earth surface emissivity, i.e.,  $LSE_{\text{SP}}$ ), produced and provided by the Earth Remote Sensing Data Analysis Center (ERSDAC). These standard products are generated based on the TES algorithm developed by Gillespie et al. (1998). Since ASTER is not able to measure atmospheric parameters, external information is required to remove the atmospheric contribution to the at-sensor radiance. To this end, information from sources such as the National Centers for Environmental Prediction–National Center for Atmospheric Research (NCEP–NCAR) reanalysis or climatology data from the Naval Research Laboratory (NRL) are introduced into the MODTRAN 3.5 radiative code to estimate the atmospheric parameters (Palluconi et al. 1999).

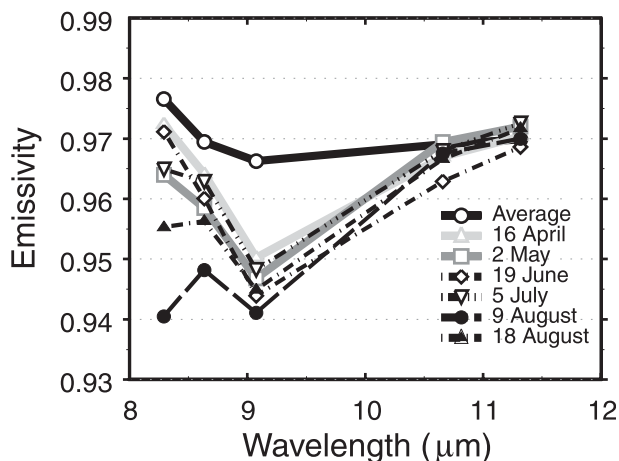


FIG. 5. Test site spectral emissivity obtained by means of the TES product (AST05) for each day and the average spectrum obtained from laboratory and field measurements.

In this study we used ASTER standard products that were atmospherically corrected by means of the NRL data, thus allowing us the possibility to study the effects of uncertainties in atmospheric characterization introduced by climatology data during such low-humidity conditions, where slight errors in water vapor content may yield important relative errors that impact the atmospheric corrections.

In Table 4,  $11 \times 11$  pixel average surface temperatures for the 6 days are shown, as well as discrepancies with the ASTER TES LST and  $LST_{\text{ground}}$  results. The standard products provided results similar to those of the TES-implemented ones, with an RMSD of 0.8 K, showing the better results for days characterized by low atmospheric water vapor content.

With regard to the emissivity, Fig. 5 shows the average emissivity for the test zone as well as the  $11 \times 11$  pixel surface emissivity for the 6 days, which presents the same underestimation trend as the TES method reported upon in Table 3 and Fig. 4. This result led us to consider more seriously the surface roughness effect as being the cause of the lower emissivity retrieved. Figure 5 also shows how the emissivity spectra from the standard products behave unevenly between the night and day data, while the emissivities from the TES method are consistent between the 6 days. Moreover, the MMDs obtained by means of the standard products are slightly lower than those in the previous section (from 0.022 to 0.027) for the day scenes, and slightly higher (0.030 and 0.027) for the night ones. Table 5 shows how bands 13 and 14 provide the best results, which are comparable to those obtained previously (LSE in Table 3). The emissivities in bands 10 and 11 also show a good level of performance for the day data, within the threshold of  $\pm 0.015$ , while

TABLE 5. Differences between surface emissivity measured with CE2 and the box method and those obtained by means of the ASTER product AST05 for each ASTER band for the 6 days.

Day	Band 10	Band 11	Band 12	Band 13	Band 14
16 Apr	0.004	0.005	0.016	0.002	-0.001
2 May	0.012	0.011	0.019	-0.000	-0.002
19 Jun	0.005	0.009	0.022	0.006	0.001
5 Jul	0.012	0.007	0.018	0.001	-0.003
9 Aug	0.036	0.021	0.025	0.001	-0.001
18 Aug	0.021	0.013	0.021	0.002	-0.002
RMSD	0.019	0.012	0.021	0.003	0.002

important deviations occur for the night data. Although the band 12 fluctuations were reduced slightly for the day data, they are still higher than the specified threshold. In this case, the worst agreement (from 0.013 to 0.036 for bands 10–12) was found in the night data, where there was greater water vapor content.

The poorer performance of the ASTER standard products obtained during days with higher water vapor content shows the failure of the climatology data to accurately reproduce the atmospheric conditions, especially in the night data, when validation exercises become more accurate and suitable (Prata et al. 2000; Wan et al. 2007).

## 6. Conclusions

ASTER TES LST and LSE estimates were evaluated by means of ground measurements concurrent with satellite data, laboratory information, and ASTER standard products for a high-elevation and low spectral contrast area located at a volcanic site on Tenerife Island, Spain. Data correspond to six scenes: four days (16 April, 2 May, 19 June, and 5 July 2008) and two nights (9 and 18 August 2008). The impacts of the external sources of error on the ASTER TES algorithm, often related to calibration and atmospheric inaccuracies, and spatial and thermal heterogeneities at sensor scales, were reduced by selecting this test site. It is nearly flat and homogeneous in both its rock composition and temperature, and presents optimal climate features, the latter because most of the water vapor is concentrated below the test site altitude throughout the whole year. A study of atmospheric characterization revealed a notably reduced atmospheric effect, relating to a sea level validation site, especially for ASTER bands 10 and 11. This reduction in the atmospheric effect was quantified, showing an increase of up to 37.1% (band 10) for atmospheric transmittance and a decrease of nearly 31.0% (band 10) for the downward and the upward atmospheric radiation. The lowest reduction in atmospheric

transmittance was found for band 12, which, as a result, was expected to display a more pronounced impact of the atmospheric correction. On the other hand, a minimum impact of the atmospheric downward radiances in all bands was expected to occur according to the results obtained in this study.

For the six ASTER scenes, level 1B (radiance at sensor) data were used. The data were calibrated by RCC versions 3.07 and 3.08 by means of a day-by-day regressive method developed by Sakuma et al. (2005), which ensures that calibration inaccuracies are small (i.e., within the threshold of ASTER–TIR radiometric noise), although the fast degradation rate that band 12 has undergone since the launch is worth mentioning (Tonooka et al. 2004).

Reference LSTs were extracted from ground measurements, carried out as part of a field campaign developed at the test site coincident with satellite overpasses, while surface emissivity was extracted from laboratory and in situ measurements using the box method.

Despite an underestimated trend obtained on most days and in most bands, a good level of agreement in the surface emissivities was shown for ASTER bands 13 and 14, where laboratory data are in tune with TES LSE (values of about 0.001 and 0.002, respectively). We attribute this underestimation to the presence of a roughness effect at scales of millimeters to centimeters, in addition to a not completely negligible atmospheric effect and calibration problems, which are responsible for the wavelength dependence of these differences. Fluctuations within the standard performance of ASTER TES were found for bands 10 and 11 (0.014 and 0.015). However, an out-of-threshold value of 0.024 was found for band 12. A greater impact of the atmospheric characterization (we found band 12 to be the least favored by the site altitude) and/or the calibration problems that arose in this band since the launch may be the cause of these significant differences. These uncertainties imply the propagation of radiometric noise inside the algorithm, which can be larger than the contrast itself, having a profound impact on surfaces characterized by a low spectral contrast. Another result to highlight is the consistency of the emissivity spectra obtained for the 6 days, for both day and night data.

With regard to the surface temperature, a comparison between ground–laboratory measurements and satellite results revealed an RMSD value of 0.5 K. The laboratory–field and ASTER standard product information comparison showed similar performance for the ASTER TES results, both in terms of surface temperature and emissivity. In fact, the same underestimated emissivity spectra retrieved by means of the standard products led us to reaffirm the presence of a roughness effect at field

and laboratory measurements scales, which was not present at ASTER scales. The failure of the emissivity retrieved under higher atmospheric water vapor content conditions points to the inability of the climatologic data used for our standard products (NRL) to represent properly the atmospheric state, especially at night, when the validation studies are more accurate and suitable due to the fact that the surface behaves almost as an isothermal and homogeneous body (Prata et al. 2000; Wan et al. 2007). Moreover, the uneven performance between the night and day data also points to a lack of precision in the standard products involved in night data retrievals.

Thus, while LST validation showed a good level of agreement between the satellite-inferred and ground data temperatures, the disagreements in the emissivity spectra retrieved indicate the presence of a cavity effect, implying a satellite-retrieved emissivity spectrum lower than that measured at the laboratory and field scales. Calibration and atmospheric characterization inaccuracies, which deeply impact the band 12 data, may be the cause of the artificial gain in contrast retrieved in this study and thus the wavelength dependence of these differences.

These results should provide useful information for ASTER users, which points to the inability of the TES algorithm to obtain LSEs within the specified threshold of  $\pm 0.015$  for low contrast surfaces even when external errors are maximally reduced, as in this case study. Thus, the assumptions involved in the TES separation algorithm need to be studied in more depth, being better adapted to these types of surfaces, and the calibration errors in band 12 cannot be ignored. Although it is worth mentioning that this study involves only one surface type and may not be statistically representative of the performance of the TES algorithm over other low-contrast surfaces, it has paved the way to a better understanding of the uncertainties involved in ASTER LST and LSE. In addition, since the performance of the TES algorithm requires further validation procedures in test sites minimally affected by atmospheric absorption/emission processes, such as that proposed here, this study will be extended to include information from a wider variety of volcanic samples located at the same altitude and close to the site selected for this study.

*Acknowledgments.* This work was supported by the Ministry of Education and Science (CGL2007-66888-C02-01/CLI) and the autonomous government of the Canary Islands (Project PI042005/108) of Spain. We are thankful to the Las Cañadas del Teide National Park for allowing us to develop all of the measurements and samples extraction in such a protected area. We also appreciate the comments made by the reviewers of

the manuscript, and we especially wish to thank Dr. T. Schmugge for his comments, which enabled us to substantially improve this manuscript.

## REFERENCES

- Ablay, G. J., M. R. Carroll, M. R. Palmer, J. Marti, and R. S. J. Sparks, 1998: Basanite-phonolite lineages of the Teide-Pico Viejo volcanic complex, Tenerife, Canary Islands. *J. Petrol.*, **39**, 905–936.
- Arai, K., 2005: Radiometric performance evaluation of ASTER VNIR, SWIR and TIR. *IEEE Trans. Geosci. Remote Sens.*, **43**, 2725–2732.
- Berk, A., and Coauthors, 1999: Modtran 4 user's manual. Air Force Research Laboratory, Space Vehicles Directorate, Air Force Materiel Command, Hanscom AFB, MA, 95 pp.
- Coll, C., and Coauthors, 2005: Ground measurements for the validation of land surface temperatures derived from AATSR and MODIS data. *Remote Sens. Environ.*, **97**, 288–300.
- , V. Caselles, E. Valor, R. Niclós, J. M. Sánchez, J. M. Galve, and M. Mira, 2007: Temperature and emissivity separation from ASTER data for low spectral contrast surfaces. *Remote Sens. Environ.*, **110**, 162–175.
- Gillespie, A. R., T. Matsunaga, S. Rokugawa, and S. J. Hook, 1998: Temperature and emissivity separation from Advanced Spaceborne Thermal Emission and Reflection Radiometer (ASTER) images. *IEEE Trans. Geosci. Remote Sens.*, **36**, 1113–1125.
- Gustafson, W. T., A. R. Gillespie, and G. Yamada, 2006: Revisions to the ASTER temperature/emissivity separation algorithm. *Proc. Second Recent Advances Quantitative Remote Sensing*, Valencia, Spain, University of Valencia, 770–775.
- Hook, S. J., R. G. Vaughan, H. Tonooka, and S. G. Schladow, 2007: Absolute radiometric in-flight validation of mid infrared and thermal infrared data from ASTER and MODIS on Terra Spacecraft using the Lake Tahoe, CA/NV, USA, automated validation site. *IEEE Trans. Geosci. Remote Sens.*, **45**, 1798–1807.
- Jimenez-Muñoz, J. C., J. A. Sobrino, A. R. Gillespie, D. Sabol, and W. T. Gustafson, 2006: Improved land surface emissivity over agricultural areas using ASTER NDVI. *Remote Sens. Environ.*, **103**, 474–487.
- Kirkland, L., K. Herr, E. Keim, P. Adams, J. Salisbury, J. Hackwell, and A. Treiman, 2002: First use of an airborne thermal infrared hyperspectral scanner for compositional mapping. *Remote Sens. Environ.*, **80**, 447–459.
- Legrand, M., C. Pietras, G. Brozniez, M. Haeffelin, N. K. Abuhassan, and M. Sicard, 2000: A high-accuracy multiwavelength radiometer for in situ measurements in the thermal infrared. Part I: Characterization of the instrument. *J. Atmos. Oceanic Technol.*, **17**, 1203–1214.
- Palluconi, F., G. Hoover, R. Alley, M. Jentoft-Nielsen, and T. Thompson, 1999: ASTER standard atmospheric correction algorithm: An atmospheric correction method for ASTER thermal radiometry over land. ASTER Algorithm Theoretical Basis Doc., Rev. 3, Jet Propulsion Laboratory, Pasadena, CA, 28 pp. [Available online at [http://eospsoc.gsfc.nasa.gov/eos\\_homepage/for\\_scientists/atbd/docs/ASTER/atbd-ast-05.pdf](http://eospsoc.gsfc.nasa.gov/eos_homepage/for_scientists/atbd/docs/ASTER/atbd-ast-05.pdf).]
- Prata, A. J., G. Rutter, M. Lynch, B. McAttee, and B. Cechet, 2000: Validation of remotely sensed thermal infrared data and surface temperature algorithm development. CSIRO Atmospheric Research Progress Rep., Aspendale, VIC, Australia, 35 pp. [Available online at [http://www.cossa.csiro.au/tasks/task2\\_4/EOCProp1\\_Report.pdf](http://www.cossa.csiro.au/tasks/task2_4/EOCProp1_Report.pdf).]

- Rubio, E., V. Caselles, C. Coll, E. Valor, and F. Sospedra, 2003: Thermal-infrared emissivities of natural surfaces: Improvements on the experimental set-up and new measurements. *Int. J. Remote Sens.*, **24**, 5379–5390.
- Sabol, D., A. R. Gillespie, E. Abbott, and G. Yamada, 2009: Field validation of the ASTER temperature–emissivity separation algorithm. *Remote Sens. Environ.*, **113**, 2328–2344.
- Sakuma, F., H. Tonooka, N. Ohgi, and H. Ono, 2005: Prediction of the radiometric calibration coefficients of ASTER/TIR. *Proc. SPIE*, **5978**, 277–284.
- Tonooka, H., F. Sakuma, M. Kudoh, and K. Iwafune, 2004: ASTER/TIR onboard calibration status and user-based recalibration. *Proc. SPIE*, **5234**, 191–201.
- , F. Palluconi, S. Hook, and T. Matsunaga, 2005: Vicarious calibration of ASTER thermal infrared bands. *IEEE Trans. Geosci. Remote Sens.*, **43**, 2733–2746.
- Wan, W., S. Liang, and T. Meyers, 2007: Validating MODIS land surface temperature using long-term nighttime ground measurements. *Remote Sens. Environ.*, **112**, 623–635.